



Published in final edited form as:

J Am Chem Soc. 2022 February 23; 144(7): 3210–3221. doi:10.1021/jacs.1c13108.

Cooperative Activation of CO₂ and Epoxide by a Heterobinuclear Al-Fe Complex via Radical Pair Mechanisms

Soumen Sinhababu^{†,a}, Maxim R. Radzhabov^{†,a}, Joshua Telser^b, Neal P. Mankad^{†,a}

^aDepartment of Chemistry, University of Illinois at Chicago, 845 W. Taylor St., Chicago, Illinois 60607, United States

^bDepartment of Biological, Physical and Health Sciences, Roosevelt University, Chicago, Illinois 60605, United States

Abstract

Activation of inert molecules like CO₂ is often mediated by cooperative chemistry between two reactive sites within a catalytic assembly, the most common form of which is Lewis acid/base bifunctionality observed in both natural metalloenzymes and synthetic systems. Here, we disclose a heterobinuclear complex with an Al-Fe bond that instead activates CO₂ and other substrates through cooperative behavior of two radical intermediates. The complex L^{diPP}(Me)Al-Fp (**2**, L^{diPP} = HC{(CMe)(2,6-ⁱPr₂C₆H₃N)}₂, Fp = FeCp(CO)₂) was found to insert CO₂ and cyclohexene oxide, producing L^{diPP}Al(Me)(μ:κ₂-O₂C)Fp (**3**) and L^{diPP}Al(Me)(μ-OC₆H₁₀)Fp (**4**), respectively. Detailed mechanistic studies indicate unusual pathways in which (i) the Al-Fe bond dissociates homolytically to generate formally Al^{II} and Fe^I metalloradicals, then (ii) the metalloradicals add to substrate in a pairwise fashion initiated by O-coordination to Al. The accessibility of this unusual mechanism is aided, in part, by the redox non-innocent nature of L^{diPP} that stabilizes the formally Al^{II} intermediates, instead giving them predominantly Al^{III}-like physical character. The redox non-innocent nature of the radical intermediates was elucidated through direct observation of L^{diPP}Al(Me)(OCPh₂) (**22**), a metalloradical species generated by addition of benzophenone to **2**. Complex **22** was characterized by X-band EPR, Q-band EPR, and ENDOR spectroscopies as well as computational modeling. The “radical pair” pathway represents an unprecedented mechanism for CO₂ activation.

Graphical Abstract

*Corresponding Author: npm@uic.edu.

† Author Contributions

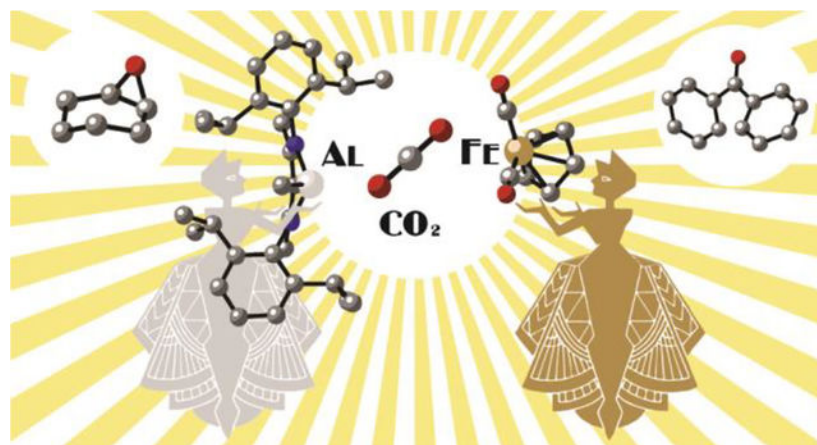
These authors contributed equally.

ASSOCIATED CONTENT

Supporting Information

The Supporting Information is available free of charge on the ACS Publications website.

Experimental procedures, spectral data, computational data (PDF)



INTRODUCTION

Identifying new reaction pathways for activation of inert substrates enables rational design of catalysts for challenging synthetic transformations. Although historically the activation of inert substrates by coordination complexes has focused on unsaturated mononuclear systems with single-site reactivity, recently there has been a resurgence in cooperative bond activation studies in which reactivity is delocalized over two or more reactive sites within a well-defined system. Examples include frustrated Lewis pairs (FLPs),¹ metal-ligand bifunctional catalysts,² homo- and heterobinuclear metal complexes,³ and multinuclear metal clusters.⁴ As a representative example, one can consider the coordination chemistry of CO₂. While CO₂ activation by mononuclear metal complexes has been mapped extensively,⁵ remaining challenges in catalytic CO₂ fixation have motivated numerous studies on cooperative CO₂ activation.⁶ The dominant paradigm is one of Lewis acid/base bifunctionality (Figure 1a): a Lewis basic reactive site adds a reactive electron pair to the carbon center of CO₂, while the resultant buildup of negative charge on oxygen is simultaneously stabilized by a Lewis acidic reactive site.⁷ Since the seminal work of Floriani on cooperative CO₂ activation by low-valent Co/M bifunctional systems (M = alkali metal),⁸ numerous examples of metal- and non-metal-based systems functioning by this paradigm have been identified.⁹ Moreover, Lewis acid/base bifunctionality is thought to be the operative paradigm in nature, stabilizing CO₂-activated intermediates in both aerobic (Mo/Cu) and anaerobic (Ni/Fe) carbon monoxide dehydrogenase enzymes.¹⁰ Identifying reaction pathways beyond this prevailing CO₂ activation manifold has the potential to open new catalyst design strategies.¹¹

In this report, we disclose a system that activates CO₂ and other substrates by a radical pair mechanism, which is a novel mechanistic paradigm for cooperative CO₂ reactivity (Figure 1b). In our discovered system, a heterobinuclear complex dissociates homolytically to generate two metalloradical intermediates, which then cooperatively activate CO₂ as a radical pair that donates one electron per metal. In part due to the unfavorable one-electron reduction potential of CO₂ ($E^{\circ} = -1.9$ V at pH 7), activation of CO₂ by metalloradical pairs is quite rare. In the cases that have been observed, generation of high-energy radical pairs required photochemical or electrochemical activation of a precursor complex.^{12a} The

concept of frustrated radical pairs has recently emerged in the field of FLP chemistry,^{12b-d} but typically such systems are limited to activation of relatively weak bonds (e.g. H-SnR₃, RO-OR) or substrates possessing radical character of their own (e.g. O₂, TEMPO). On the contrary, here the heterobimetallic radical pair is capable of cooperatively activating not only CO₂ but also the C-O bond of an epoxide under ambient conditions with no external stimulus.

As detailed below, our discovery emerged from studies of an Al-Fe heterobinuclear system. Despite extensive recent work on heterobimetallic chemistry,¹³ heterobimetallic complexes bearing aluminum (Earth's most abundant metal) are not thoroughly studied and their reactivity remains underexplored,¹⁴ especially for heterobimetallic complexes in which aluminum is paired with another earth-abundant metal.¹⁵⁻²⁰ Only a few examples of cooperative CO₂ activation by Al/M heterobinuclear complexes have been reported, with their mechanistic pathways currently under debate in some cases. In 2019, Goicoechea and Aldridge reported CO₂ insertion into an Al-Au bond (Figure 2a).²¹ A cooperative Lewis acid/base mechanism involving nucleophilic auride (i.e., Al^{III}-Au^{-I}) was proposed initially, although recent theoretical analysis by Sorbelli et al. disfavors that proposal and instead supports diradical-like reactivity (i.e., Al^{II}-Au⁰).²² In 2021, Frenking, Goicoechea, and Aldridge disclosed analogous reactivity of the Al-Cu and Al-Ag derivatives (Figure 2a), again proposing Lewis acid/base mechanisms.²³ A closely related set of Al-Cu reactions with CO₂ were reported by Hill and McMullin in 2021 (Figure 2b).¹⁸ In 2021, Goicoechea and Aldridge reported CO₂ insertion into an Al-Zn bond (Figure 2c), although no mechanistic studies were reported.²⁴ Finally, in 2021, Camp reported CO₂ deoxygenation by a Al^{III}-Ir^{III} complex that was proposed to go by a concerted transition state (Figure 2d).^{9e}

We became interested in pursuing the chemistry of Al-Fe complexes, particularly those derived from Al^{III} rather than Al^I precursors. Despite aluminum and iron being the two most abundant metals in earth's crust (7.4% and 5%, respectively), only a few Al-Fe heterobimetallic complexes have been reported and their reactivity has never been studied.^{15,16,25} Herein we report that the β -diketiminate-supported Al-Fe heterobimetallic complex, L^{dipp}(Me)Al-FeCp(CO)₂ (L^{dipp} = HC{(CMe)(2,6-*i*-Pr₂C₆H₃N)}₂), is able to insert CO₂ and cyclohexene oxide. Using a combined experimental/computational approach, the reaction pathways for CO₂ activation and epoxide ring opening were elucidated to involve (i) homolytic Al-Fe dissociation to metalloradical intermediates, then (ii) pairwise addition to substrate prior to solvent cage escape. This "radical pair" mechanism is a novel mode of cooperative CO₂ activation, and its extension to epoxide ring-opening may open new avenues for C-O activation.

RESULTS & DISCUSSION

Synthesis and reactivity.

To synthesize Al-Fe heterobimetallic complex L^{dipp}Al(Me)Fp (**2**, Fp = FeCp(CO)₂), reaction of L^{dipp}Al(Me)I (**1**) was carried out with KFp in a mixture of toluene and ether for 16 h (Scheme 1). Compound **2** was obtained as a colorless solid in moderate yield (66 %) and was found to be soluble in toluene and diethyl ether but to decompose in tetrahydrofuran,

chloroform, and dichloromethane. Furthermore, solutions of **2** in toluene slowly decay to produce Fp_2 over extended periods of time at room temperature.

Reactions of **2** with CO_2 and epoxide were carried out since they are both useful feedstocks for preparation of cyclic or polycarbonate products, often with the involvement of Al catalysts.²⁶ Accordingly, reaction of compound **2** with CO_2 in toluene resulted in CO_2 -inserted product $\text{L}^{\text{diPP}}\text{Al}(\text{Me})(\mu:\kappa_2\text{-O}_2\text{C})\text{Fp}$ (**3**) as a colorless solid in 81% yield (Scheme 1). This reaction was found to occur with equal efficiency when shielded from light. Insertion of CO_2 into Al-M bonds with κ_2 binding to Al is rare, with previously reported examples involving low valent Al^{I} rather than Al^{III} precursors.^{18,21,23,24} Compound **3** was stable to thermolysis and vacuum exposure, and we observed no evidence for conversion back to **2** under these conditions. In the $^{13}\text{C}\{^1\text{H}\}$ NMR spectrum of **3**, the carbon atom of the $[\kappa_2\text{-O}_2\text{C}]$ moiety resonates at 220.8 ppm, which is shifted downfield compared to the bridging CO_2 unit in $[\text{Cp}_2\text{Zr}(\text{Cl})(\mu:\kappa_2\text{-O}_2\text{C})\text{FeCp}(\text{CO})_2]$ ($\delta=212.6$ ppm).²⁷ Stoichiometric reaction of **2** with cyclohexene oxide was carried out at room temperature, resulting in ring-opened product $\text{L}^{\text{diPP}}\text{Al}(\text{Me})(\mu\text{-OC}_6\text{H}_{10})\text{Fp}$ (**4**, 57 %, Scheme 1). Ring opening of epoxides using Al/Co heterobimetallic catalysts has been proposed by the Coates group for several carbonylation reactions,²⁸ but such an intermediate has never been isolated until now. Compound **4** is stable at -25 °C but decomposes slowly at room temperature inside the glove box. The solid-state IR spectrum of **2** has features at 1903 and 1963 cm^{-1} assigned to the CO ligands that are shifted to higher energy in **3** (1981, 2021 cm^{-1}) and **4** (1935, 2002 cm^{-1}), corresponding with a change in formal Fe oxidation state from Fe(0) to Fe(II).

The molecular structures of **2** and **4** feature four-coordinate aluminum centers with distorted tetrahedral geometries, while **3** has a penta-coordinate aluminum center with distorted square pyramidal geometry, as determined by X-ray crystallography. The Fe-Al bond length [2.478(9) Å] in **2** is comparable to the value of 2.480(1) Å reported for the related compound $\text{L}^{\text{diPP}}\text{Al}(\text{Cl})\text{Fp}^*$ ($\text{Fp}^* = \text{Cp}^*\text{Fe}(\text{CO})_2$; $\text{Cp}^* = \text{C}_5\text{Me}_5$)^{25c} but longer than the other previously reported Fe-Al bonds (2.231(3)-2.349(9) Å).^{25d-25f} The Al-O bond lengths in **3** [1.980(1) and 1.897(1) Å] are slightly longer to the corresponding bonds [1.880(5) and 1.861(4) Å] present in $(\text{NON})\text{Al}(\kappa_2\text{-O}_2\text{C})\text{AuP}^*\text{Bu}_3$ ($\text{NON} = 4,5\text{-bis}(2,6\text{-diisopropylanilido})\text{-}2,7\text{-di-tert-butyl-}9,9\text{-dimethylxanthene}$).²¹ The O-C bond lengths for the $\text{Al}(\kappa_2\text{-O}_2\text{C})\text{Fe}$ unit in **3** [1.271(2) and 1.298(2) Å] fall between the typical ranges for C-O single and double bonds. The Fe-C bond [1.933(1) Å] of the $\text{Al}(\kappa_2\text{-O}_2\text{C})\text{Fe}$ unit is comparable with the Fe-C bond [1.935(14) Å] seen in $\text{HC}(\text{SiMe}_2\text{NC}_6\text{H}_4\text{F-}2)_3\text{-Zr}(\kappa_2\text{-S}_2\text{C})\text{Fe}(\text{CO})_2\text{Cp}$.²⁹ The molecular structure of **4** reveals that $\text{LAl}(\text{Me})\text{O}$ and Fp moieties are in *trans* orientation about the cyclohexane unit. The Al-O bond length [1.728(2) Å] in **4** is much shorter than those in **3**. The Fe- C_{Cy} bond length is 2.111(3) Å, which is in range of reported Fe- C_{alkyl} bonds.³⁰

Complex **3** is stable thermally (up to 60 °C) in C_6D_6 for at least 12 h but was found to react further upon irradiation with UV light. A C_6D_6 solution of **3** was irradiated at ambient temperature for 5 h. The ^1H NMR spectrum reveals complete conversion of **3** to **5** (Scheme 1). In the ^1H NMR spectrum of compound **3**, the Al- CH_3 protons appear as a singlet at -0.20 ppm but are shifted downfield to 1.71 ppm in **5**, indicating methyl migration from the aluminum center to the ligand backbone. The crystal structure of **5**

revealed that its aluminum center is tetra-coordinate with two nitrogen and two oxygen atoms in its immediate environment. It also confirmed that the methyl group migrated from aluminum to the β -diketiminato backbone as anticipated from ^1H NMR spectroscopy. The methyl migration to the β -diketiminato ligand transforms it into a dianionic ligand. Although the M-C bond migration phenomenon has been observed in transition metal β -diketiminato chemistry, this is first report involving an aluminum β -diketiminato.^{31,32} The $\text{C}_3\text{N}_2\text{Al}$ six membered ring is puckered with both Al-N bonds being almost equal in distance [1.774(3) Å and 1.808(3)]. The Al-O bond lengths [1.862(2) Å and 1.848(2)] are shorter than in **3**, possibly due to change in coordination number at the aluminum center.

Computational analysis of atomic charges & bonding.

To better understand the origins of reactivity of our Al-Fe heterobimetallic complex $\text{L}^{\text{dipp}}\text{Al}(\text{Me})\text{Fp}$ (**2**), we decided to study the charge distribution using NBO³³ (Figure S18) and QTAIM³⁴ (Figure 3) analysis methods on pre-optimized geometries for complex **2** and, for modelling purposes, its simplified counterparts with methyl ($\text{L}^{\text{Me}}\text{Al}(\text{Me})\text{Fp}$, **6**) and phenyl ($\text{L}^{\text{Ph}}\text{Al}(\text{Me})\text{Fp}$, **7**) substituents in place of 2,6-diisopropylphenyl (dipp) in **2**. QTAIM charges, being origin-independent³⁵ and more “chemically intuitive”, are consistent with representation of complexes **2**, **6** and **7** as featuring strongly polarized covalent $\text{Al}^{\text{III}}\text{-Fe}^0$ bonds. For comparison, we also calculated NBO and QTAIM charges for a well-studied heterobimetallic system,³⁶ $\text{Me}^{\text{IMes}}\text{CuFp}$ **8** ($\text{Me}^{\text{IMes}} = 1,3\text{-bis}(2,4,6\text{-trimethylphenyl})\text{-4,5-dimethylimidazol-2-ylidene}$, Figures S18 and 3). QTAIM charges in this model system are much closer to traditional ideas of valence, with Cu being in the oxidation state of (almost) one and Fe being in the oxidation state of zero.

To further confirm the presence of the covalent bond between two metals, we calculated Wiberg bond indices (WBIs) in Löwdin orthogonalized basis³⁷ (Figure 3 and Table S1). From the obtained data we can conclude that the Al-Fe bond in **2** is almost twice as covalent as the Cu-Fe bond in **8**. Thus, some caution must be used in describing the oxidation levels of the Al and Fe centers in **2**.

Although the used methods gave quite differing charge values, trends between structures in question are consistent. This allowed us to (initially) simplify our model and study Me-substituted complex **6** in lieu of complex **2** to study its reactivity *in silico* towards CO_2 insertion and epoxide ring opening at a lower computational cost.

Combined computational/experimental investigation of reaction mechanisms.

We decided to begin with calculating energies for two dissociation pathways (Scheme 2a), homolytic and heterolytic, for truncated model complexes **6** and **7**. However, dissociation energies for both **6** and **7** proved to be too high, even when including effects of the toluene solvent. It is worth noting that Gibbs free energies and enthalpies are significantly (>20 kcal/mol) lower for homolytic rather than heterolytic dissociation. Steric bulkiness of substituents (i.e. Me vs Ph) appeared irrelevant: for homolytic dissociation both G_{d} and H_{d} were just ~6 kcal/mol lower for significantly bulkier **7**, and for heterolytic dissociation Gibbs free energies and enthalpies for **7** were even higher than for **6**. Therefore, we decided not to proceed with dissociation calculations for complex **2**, a decision that later proved imprudent.

Since calculated dissociation energies were inconsistent with reactions that occur readily at ambient conditions, we decided to explore possible mechanistic pathways beginning with the concerted CO₂ insertion (Scheme 2b) via the corresponding transition state (TS). Obtained Gibbs free energies indicated that while the CO₂ insertion *per se* is thermodynamically favorable, the concerted pathway's high activation barrier is also inconsistent with a reaction that occurs with reasonable rate at room temperature (as observed experimentally). To make sure the obtained TS energy was not an artifact of poorly chosen DFT functional, we recalculated the transition state energy using several DFT functionals (Figure S17). Obtained Gibbs free energies are generally consistent among all employed functionals, which indicates that such a high obtained value is not an error of the chosen functional.

To gain additional insights on the mechanism, we next conducted an Eyring analysis by obtaining experimental, pseudo-first order (excess CO₂) rate constants for CO₂ activation by **2** across the temperature range 263–303 K (Figure 4). Fitting the data to the Eyring equation provided the experimentally determined activation parameters for CO₂ insertion by complex **2**: $H^\ddagger = 26 \pm 2$ kcal/mol, $S^\ddagger = 24 \pm 7$ cal/mol*K, $G^\ddagger_{298K} = 19 \pm 3$ kcal/mol. The activation entropy for this reaction is large and positive, which indicates a dissociative rate-determining step and is therefore inconsistent with the concerted mechanism shown in Scheme 2b (which should give $S^\ddagger < 0$). Moreover, the *trans*-stereochemistry of the ring-opened product **4** evident by X-ray crystallography indicates *anti*-addition of the two metals to the epoxide and thus also testifies against any similar concerted mechanisms.

With these considerations in mind, we decided to revisit the dissociation pathways, this time with the model for **2** with full-sized dipp-substituted ligands (Scheme 3). To our surprise, the dissociation Gibbs free energies and enthalpies were ~15 kcal/mol lower than for closest counterpart **7**. This brought the activation barrier down, closer to the experimental value and within the expected range for a room-temperature reaction. Therefore, *relying on models with truncated substituents, a common approach in computational organometallic chemistry, is not always justified*. It is curious that addition of just two isopropyl groups to each phenyl ring had such drastic effect on dissociation energies, which we attribute solely to significantly higher steric repulsion in complex **2** relative to **6** and **7**, given their similar electronic structures. Although the homolytic dissociation energy for **2** is similar to the calculated barrier for concerted CO₂ activation by **6**, a dissociative mechanism would better align with the experimental Eyring analysis for CO₂ reactivity of **2**. Also noteworthy is the *trans* geometry of epoxide activation product **4**, rather than the *cis* configuration expected from a concerted, four-membered transition state for C-O cleavage at the Al-Fe bond. Collectively, these observations also reinforce *the critical importance of calibrating computed mechanisms with experimental (preferably kinetics) data*.

With further evidence towards homolytic dissociation of complex **2** as the origin of its reactivity and having ruled out several alternatives (Figure S17), we calculated the Gibbs free energies of interactions of both Al and Fe metalloradicals with both CO₂ and cyclohexene oxide. As follows from the obtained Gibbs energies, both CO₂ and cyclohexene oxide prefer to react with the Al radical [L^{dipp}AlMe]• (**15**) rather than with Fe radical Fp• (**16**), as indicated in Scheme 4. In the first case, for CO₂ insertion, we could

not localize a minimum corresponding to the radical $[\text{FpCO}_2]\cdot$ complex **19**. (However, we were able to localize a minimum for a similar anionic complex, which has been observed experimentally³⁸; see SI for more details.) Instead, the localized minimum was a supramolecular complex **19'** of Fp radical **16** and CO_2 , held together by weak non-covalent bonds (as shown by QTAIM diagrams and calculated WBIs; Figure 5a). However, we localized a minimum for the complex **17** where a linear CO_2 molecule is coordinated on the Al center of complex **15**, giving a quite strong covalent bond (also Figure 5a). Such coordination is endothermic, but the subsequent interception of Fp radical **16** makes CO_2 insertion a thermodynamically favorable process.

Epoxide ring opening is also an exothermic process even for initiation with the Al radical **15**, while initiation by Fe radical **16** has a very high barrier (Scheme 5). Subsequent recombination of Al-epoxide complex **21** with **16** to give the observed product **4** is energetically very favorable.

The identification of the O-bound CO_2 adduct **17** along the reaction pathway is notable, as this coordination mode has rarely been observed experimentally³⁹ and is typically proposed during (1-electron) reductive coupling of CO_2 to form oxalate⁴⁰ (rather than for 2-electron CO_2 reduction). Moreover, it is a rare example of a formally Al^{II} species playing an important role in reactivity.⁴¹ Thus, we chose to analyze the electronic structure of **17** and its precursor complex **15** further. Calculated Mulliken spin densities for selected atoms (Figure 5b) of these complexes indicate that the unpaired electron is mostly delocalized through the conjugated β -diketiminate ligand but not on Al itself for either complex, nor on the CO_2 moiety in the case of **17**. In other words, although **15** is *formally* a $[(\text{L}^{\text{diPP}})^-]\text{Al}^{\text{II}}\text{Me}$ species, it is perhaps better formulated as $[(\text{L}^{\text{diPP}})^{2-}]\text{Al}^{\text{III}}\text{Me}$ and thus possess a vacant Al-centered $3p_z$ orbital for substrate coordination. This dual radical/acid character of **15** is critical to successful activation of CO_2 , which otherwise resists participating in radical chemistry due to its unfavorable one-electron reduction potential ($E^\circ = -1.9$ V at pH 7).

Experimental validation of the radical pair mechanism.

Given these computational results indicating an unusual radical pair mechanism for the cooperative bond activation chemistry of **2**, we sought experimental validation of the computational predictions. One notable prediction from computational modeling is that the homolytic Al-Fe bond dissociation energy in $\text{L}^{\text{Ph}}\text{Al}(\text{Me})\text{Fp}$ (**7**) should be higher than that in $\text{L}^{\text{diPP}}\text{Al}(\text{Me})\text{Fp}$ (**2**) by 18 kcal/mol. Thus, radical pair generation from **7** should not proceed under the mild conditions at which reactivity of **2** was observed. Indeed, exposure of **7** to CO_2 resulted in no reaction (Scheme 6a) under conditions at which **2** activated CO_2 rapidly (Scheme 1). This observation provides experimental confirmation of a key prediction of our computational modeling.

Next, we sought further evidence for formation of metalloradicals **15** and/or **16** under relevant conditions by screening reactions with other substrates with C-O or C=O bonds. Fortuitous results were obtained from the reaction of **2** with benzophenone (Scheme 6b). Addition of benzophenone to **2** at room temperature results in an intense, purple-colored solution. Analysis of this solution by ^1H NMR spectroscopy indicates stoichiometric

formation of Fp_2 , which presumably forms from dimerization of **16**. The aluminum-containing product was NMR silent, indicating a paramagnetic species. Indeed, analysis of the solution by EPR spectroscopy provided evidence for a $S = 1/2$ species assigned as $\text{L}^{\text{dipp}}\text{Al}(\text{Me})(\text{OCPh}_2)$ (**22**), which can be viewed as the benzophenone analogue of CO_2 adduct **17**. Concentrating solutions of **22** or attempting to crystallize it resulted in white-colored solids that have the same empirical formula as **22** according to elemental analysis. At this time, the identity of these solids is unclear, but they likely represent a dialuminum structure resulting from homocoupling of radical **22**, as has been observed previously by Thomas for a metalloradical-benzophenone system.⁴² Reconstitution of the white solid in toluene restores the purple color of **22**, indicating that the presumed homocoupling process is reversible and is driven towards the monomeric radical in solution and the dimeric, diamagnetic species in the solid state.

Next, we analyzed the electronic structure of **22**, in a manner similar to **17** and **19'**. QTAIM analysis of the localized minimum for **22** revealed a highly covalent Al-O bond (Figure 6a). Calculated WBIs (also Figure 6a) showed that benzophenone's C=O bond loses its double bond character ($\text{WBI} = 1.707 < 2$), which is consistent with the IR spectrum obtained for **22** (see SI for more details). The bond between Al and O ($\text{WBI} = 1.294$) is almost three times as covalent as a similar bond ($\text{WBI} = 0.439$) in the complex with CO_2 (**17**).

Calculated Mulliken spin densities (Figure 6b) for selected atoms of **22** reveal that the unpaired spin resides predominantly on the benzophenone unit and not on the conjugated β -diketiminato ligand as was observed in the previous case with **17**, nor on Al. Therefore, **22** can be described as $\text{L}^{\text{dipp}}\text{Al}^{\text{III}}[(\text{OCPh}_2)^-]\text{Me}$, with the formerly vacant Al-centered $3p_z$ orbital occupied by benzophenone's oxygen lone pair electrons. The relation of these results with EPR experiments is discussed in the following section.

The purple toluene solution of **22** exhibits a room temperature (i.e., fluid solution) X-band EPR signal as shown in Figure 7a. The signal is at $g_{\text{iso}} = 2.006$ and comprises a Gaussian lineshape with width (hwhm) of 16 MHz. However, this does not fully describe the signal as there appears to be superimposed hyperfine splitting. This splitting can be modeled by hyperfine coupling (hfc) to one ^{27}Al ($I = 5/2$, 100% abundance) with $a_{\text{iso}} = 4$ MHz and three types of ^1H : $a_{\text{iso}} = 22$ MHz (4 equivalent nuclei), $a_{\text{iso}} = 7.5$ MHz (4 equivalent nuclei), and $a_{\text{iso}} = 26$ MHz (2 equivalent nuclei). The rationale for this parameter set, which is neither ideal nor unique will be given below. That the hfc is not fully (i.e., "baseline") resolved is explained by appearance of the EPR spectrum recorded at 80 K (i.e. in frozen solution, Figure 7b), which is overall broader due to g anisotropy (see Q-band results below) and possible hfc anisotropy as well. Here we did not even attempt to simulate any possible hfc. At 300 K, there is some rotational averaging so that hfc is partially resolved, while there is none at 200 K (not shown).

A close analog to **22** is the complex studied by Murphy et al., $\text{L}^{\text{dipp}}\text{Mg}(\text{DMAP})(\text{OCPh}_2)$, where DMAP = 4-dimethylaminopyridine.⁴³ This compound can be formally described as Mg(I) with coordinated benzophenone or, more realistically, as Mg(II) with coordinated benzophenone radical anion. The X-band EPR spectrum of $\text{L}^{\text{dipp}}\text{Mg}(\text{DMAP})(\text{OCPh}_2)$ in toluene gave poorly resolved hfc at 200 K (with $g_{\text{iso}} = 2.004$), but resolution improved at

higher temperatures and already at 250 K (as well as at 298 K) gave a beautifully resolved spectrum that was perfectly simulated when accounting for accompanying ENDOR and TRIPLE (i.e., double ENDOR) spectroscopy data. In contrast, for **22**, we believe that a temperature much higher than ambient would be needed to obtain complete resolution, which could allow definitive determination of hfc in this relatively bulky molecule. Murphy et al. extracted a_{iso} values for ^{25}Mg ($I = 5/2$, 10.0%) of 5.54 MHz and ^{14}N of DMAP of 0.90 (zero from ^{14}N of L^{dipp}). Additionally, a_{iso} values for the four sets of benzophenone phenyl protons were determined as *ortho*-H¹, 8.80 MHz; *ortho*-H², 7.85 MHz; *meta*-H, 3.00 MHz; *para*-H, 10.00. This approximate ratio of benzophenone $a_{\text{iso}}(\text{o-,m-,p-}^1\text{H})$ values was used as a starting point to simulate the room-temperature X-band EPR spectrum of **22**, after scaling up to match the breadth of hfc seen for **22**. The $a_{\text{iso}}(^{27}\text{Al})$ value for **22** was estimated from ENDOR data as described in the following section. The very small value for ^{14}N hfc in the Mg complex, combined with the computational results for **22** described above, led us to ignore any possible hfc from ^{14}N .

An EPR spectrum of **22** in frozen toluene solution was also recorded at 35 GHz (Q-band) at 2 K. The EPR signal is under “passage” conditions and thus has an absorption lineshape as shown in Figure 7d; Figure 7c presents a digital derivative so that a standard EPR presentation is seen.⁴⁴ No hfc was resolved at the Q-band, which is typical considering the increased microwave frequency and corresponding resonant magnetic field.⁴⁵ More importantly, the form of **22** in frozen solution appears to be slightly different in that $\mathbf{g} = [2.0027, 2.0061, 2.007]$ so that $g_{\text{avg}} = 2.0053$, as opposed to $g_{\text{iso}} = 2.006$ at high temperature. There is spin delocalization onto the ^{27}Al center as definitively shown by ENDOR spectroscopy. EPR spectra exhibiting beautifully resolved ^{27}Al hfc have been reported by Roesky and co-workers. These systems, however, can be more properly considered as Al(II) species than **22** as the reported compounds lack any moiety equivalent to a benzophenone ketyl radical. Accordingly, those complexes give much larger ^{27}Al hfc in the range of 15 – 35 MHz.⁴⁶ Very recently, Britt, Arnold, and co-workers reported X-band EPR, 35-GHz pulsed EPR, and (Davies) ENDOR spectra for $(\eta^5\text{-Cp})_2\text{Ti}(\mu\text{-}^1,^2\text{H})_2\text{Al}^1,^2\text{H}(\text{CTMS}_3)$, where $\text{CTMS}_3 = \text{C}(\text{SiMe}_3)_3$.⁴⁷ This compound is formally Ti(III)-Al(III), but could be considered to have some Ti(IV)-Al(II) character. In contrast to **22**, but as expected for Ti(III), this complex exhibits significant g anisotropy: $\mathbf{g} = [2.003, 1.992, 1.971]$, which allowed determination of not only $a_{\text{iso}}(^{27}\text{Al}) = 9.4$ MHz, but also $\mathbf{A}(^{27}\text{Al}) = [6.0, 14.6, 7.6]$ MHz.

ENDOR spectroscopy is broad banded in that signals from all magnetically active nuclei with hfc to the paramagnetic center can in principle be observed. A wide scan ENDOR spectrum of **22** recorded at $g = 2.006$ is shown in Figure 8 (main figure). Signals from ^1H are readily observed at the ^1H Larmor frequency ($\nu_{\text{H}} \approx 53$ MHz). In addition to a strong signal directly at ν_{H} , which corresponds to protons with negligible hfc, there are features symmetrically disposed about it that give hfc for three types of magnetically equivalent protons, as expected for the phenyl rings of benzophenone.⁴³ These give $A(^1\text{H}) \approx 4, 10,$ and 15 MHz, as seen in Figure 8 (right inset). These values are smaller than the three $a_{\text{iso}}(^1\text{H})$ values used in the 300 K fluid solution X-band EPR simulation. This may be due to the difference between fluid and frozen solution in that the features seen by ENDOR may each

be only one component ($\sim A_{\perp}$) of an anisotropic, indeed highly dipolar, hfc tensor: $\mathbf{A}({}^1\text{H}) = [a_{\text{iso}} \pm (T - \rho), a_{\text{iso}} \pm (T + \rho), a_{\text{iso}} \mp 2T]$.

An additional feature is seen at ~ 14 MHz that corresponds exactly to the ${}^{27}\text{Al}$ Larmor frequency. This signal recorded at two field positions, corresponding roughly to g_{\parallel} and g_{\perp} , is shown in Figure 8 (left inset). This feature provides the rough estimate used for EPR simulation of $a_{\text{iso}}({}^{27}\text{Al}) = 4$ MHz. This estimate as to hfc corresponds to $\sim 0.1\%$ spin on ${}^{27}\text{Al}$.⁵⁰ The metal hfc found by Murphy et al., $|a_{\text{iso}}({}^{25}\text{Mg})| = 5.54$ MHz, corresponds to 1.14% $3s^1$ spin density.

CONCLUSIONS

Heterobimetallic Al-Fe complex, **2**, reacts cleanly with CO_2 and cyclohexene oxide, giving CO_2 inserted product **3** and epoxide ring opening product **4**, respectively. Detailed kinetic and theoretical studies were performed on these two reactions and indicated an unusual radical-pair mechanism in which Al-Fe homolytic dissociation precedes pairwise metalloradical addition to substrate. The Al-containing metalloradical coordinated by benzophenone (**22**) was observed directly and thoroughly characterized by EPR and ENDOR spectroscopies. Particularly novel aspects of this study include:

- Aluminum-containing radicals with dual radical/acid character implicated as a reactive intermediates
- An unprecedented mechanism for CO_2 activation
- An instructive interplay between theory and experiment that emphasizes the importance in computational organometallic chemistry of (i) validating calculated reaction pathways with kinetics measurements, and (ii) modeling complete (as opposed to truncated) ligand substituents

METHODS

Experimental methods.

All experimental manipulations were carried out under inert dinitrogen atmosphere using standard Schlenk line and glovebox techniques. All new compounds were characterized by ${}^1\text{H}$ and ${}^{13}\text{C}\{{}^1\text{H}\}$ NMR spectroscopy, solid-state IR spectroscopy, and single-crystal X-ray diffraction. Detailed experimental procedures and spectral data are available as Supplementary Information, and supporting crystallographic data in the form of CIF files are available upon request from the Cambridge Crystallographic Data Centre using deposition numbers 2100519, 2100520, 2100523, and 2100525.

Computational methods.

Density Functional Theory calculations (at the PBE0^{49a}-G3BJ^{49b}/def2-TZVP^{49c} level of theory; SMD^{51d} solvation model with toluene parameters), as implemented in the Gaussian 16 (Revision B.01)⁵⁰ code, were employed to optimize molecular geometries and determine bonding energies, Mulliken spin densities and NBO charges (using NBO version 3.1,⁵¹ as implemented in Gaussian 16). The open-source MultiWFN⁵² (version 3.8) program

was employed to calculate and visualize Wiberg bond indices, QTAIM charges, critical points and paths (using data derived from Gaussian DFT calculations). For more details on comprehensive computational methods please see Supplementary Information.

Supplementary Material

Refer to Web version on PubMed Central for supplementary material.

ACKNOWLEDGMENT

This material is based upon work supported by the U.S. Department of Energy (DOE), Office of Science, Office of Basic Energy Sciences (BES), under Award Number DE-SC0021055. We thank Prof. Brian M. Hoffman (Northwestern University) for use of a 35-GHz CW EPR/ENDOR spectrometer, which is supported by the US DOE, Office of Science, BES, under Award Number DE-SC0019342. Computational resources and services were provided by the Advanced Cyberinfrastructure for Education and Research (ACER) group at UIC. Instrumentation for X-ray crystallography at UIC was funded, in part, by the National Institutes of Health under grant R01 GM116820. The structure of complex **5** was obtained using NSF's ChemMatCARS Sector 15 supported by the Divisions of Chemistry (CHE) and Materials Research (DMR), National Science Foundation, under grant number NSF/CHE-1834750. Use of the Advanced Photon Source, an Office of Science User Facility operated for the DOE Office of Science by Argonne National Laboratory, was supported by the U.S. DOE under Contract No. DE-AC02-06CH11357. We thank Dr. Guodong Rao, UC-Davis, and Dr. Vlasta Brezová, Slovenská technická univerzita v Bratislave (STU), Slovakia, for helpful discussions. We also thank Dr. Daniel McElheny (UIC) for assistance with X-band EPR spectroscopy.

REFERENCES

- (1). Stephan DW The Broadening Reach of Frustrated Lewis Pair Chemistry. *Science* 2016, 354, 7229.
- (2). (a)Gunanathan C; Milstein D Metal–Ligand Cooperation by Aromatization–Dearomatization: A New Paradigm in Bond Activation and “Green” Catalysis. *Acc. Chem. Res.* 2011, 44, 588–602. [PubMed: 21739968] (b)Morris RH Exploiting Metal-Ligand Bifunctional Reactions in the Design of Iron Asymmetric Hydrogenation Catalysts. *Acc. Chem. Res.* 2015, 48, 1494–1502. [PubMed: 25897779]
- (3). (a)Campos J Bimetallic cooperation across the periodic table. *Nat. Rev. Chem.* 2020, 4, 696–702. (b)Powers IG; Uyeda C Metal-metal bonds in catalysis. *ACS Catal.* 2017, 7, 936–958.
- (4). Buchwalter P; Rose J; Braunstein P Multimetallic Catalysis Based on Heterometallic Complexes and Clusters. *Chem. Rev.* 2015, 115, 28–126. [PubMed: 25545815]
- (5). Paparo A; Okuda J Carbon Dioxide Complexes: Bonding Modes and Synthetic Methods. *Coord. Chem. Rev.* 2017, 334, 136–149.
- (6). (a)Burkart MD; Hazari N; Tway CL; Zeitler EL Opportunities and Challenges for Catalysis in Carbon Dioxide Utilization. *ACS Catal.* 2019, 9, 7937–7956. (b)Appel AM; Bercaw JE; Bocarsly AB; Dobbek H; Dubois DL; Dupuis M; Ferry JG; Fujita E; Hille R; Kenis PJA Frontiers, Opportunities, and Challenges in Biochemical and Chemical Catalysis of CO₂ Fixation. *Chem. Rev.* 2013, 113, 6621–6658. [PubMed: 23767781]
- (7). Gibson DH The Organometallic Chemistry of Carbon Dioxide. *Chem. Rev.* 1996, 9, 2063–2095.
- (8). (a)Gambarotta S; Arena F; Floriani C; Zanazzi PF Carbon dioxide fixation: bifunctional complexes containing acidic and basic sites working as reversible carriers. *J. Am. Chem. Soc.* 1982, 104, 5082–5092. (b)Fachinetti G; Floriani C; Zanazzi PF Bifunctional activation of carbon dioxide. Synthesis and structure of a reversible carbon dioxide carrier. *J. Am. Chem. Soc.* 1978, 100, 7405–7407.
- (9). (a)Hanna TA; Baranger AM; Bergman RG Reaction of Carbon Dioxide and Heterocumulenes with an Unsymmetrical Metal-Metal Bond - Direct Addition of Carbon-Dioxide across a Zirconium-Iridium Bond and Stoichiometric Reduction of Carbon Dioxide to Formate. *J. Am. Chem. Soc.* 1995, 117, 11363–11364. (b)Krogman JP; Foxman BM; Thomas CM Activation of CO₂ by a Heterobimetallic Zr/Co Complex. *J. Am. Chem. Soc.* 2011, 133, 14582–14585. [PubMed: 21875088] (c)Mömming CM; Otten E; Kehr G; Fröhlich R; Grimme S; Stephan DW; Erker G Reversible Metal-Free Carbon Dioxide Binding by Frustrated Lewis Pairs. *Angew. Chem.*,

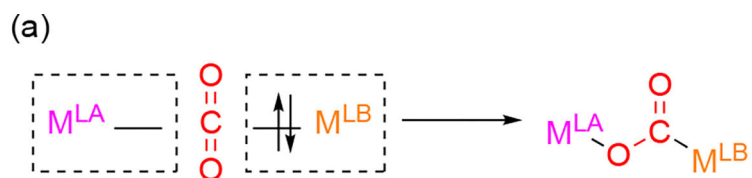
- Int. Ed. 2009, 48, 6643–6646.(d)Schlenker K; Christensen EG; Zhanserkeev AA; McDonald GR; Yang EL; Lutz KT; Steele RP; Vanderlinden RT; Saouma CT Role of Ligand-Bound CO₂ in the Hydrogenation of CO₂ to Formate at a (PNP)Mn Catalyst. *ACS Catal.* 2021, 11, 8358–8369.(e)Escomei L; Del Rosal I; Maron L; Jeanneau E; Veyre L; Thieuleux C; Camp C Strongly Polarized Iridium^{δ-}–Aluminum^{δ+} Pairs: Unconventional Reactivity Patterns Including CO₂ Cooperative Reductive Cleavage. *J. Am. Chem. Soc.* 2021, 143, 4844–4856. [PubMed: 33735575]
- (10). (a)Dobbek H; Svetlitchnyi V; Gremer L; Huber R; Meyer O Crystal Structure of a Carbon Monoxide Dehydrogenase Reveals a [Ni-4Fe-5S] Cluster. *Science* 2001, 293, 1281–1285. [PubMed: 11509720] (b)Mankad NP; Ghosh D Biomimetic Studies of the Mo/Cu Active Site of CO Dehydrogenase. *Comprehensive Coordination Chemistry III*, 2021, pp 772–789.
- (11). Karunananda MK; Mankad NP Cooperative Strategies for Catalytic Hydrogenation of Unsaturated Hydrocarbons. *ACS Catal.* 2017, 7, 6110–6119.
- (12). (a)Agarwal J; Fujita E; Schaefer HF III; Muckerman JT Mechanisms for CO Production from CO₂ Using Reduced Rhenium Tricarbonyl Catalysts. *J. Am. Chem. Soc.* 2012, 134, 5180–5186. [PubMed: 22364649] (b)Liu L; Cao LL; Shao Y; Ménard G; Stephan DW A Radical Mechanism for Frustrated Lewis Pair Reactivity. *Chem.* 2017, 3, 259–267.(c)Dasgupta A; Richards E; Melen RL Frustrated Radical Pairs: Insights from EPR Spectroscopy. *Angew. Chem., Int. Ed.* 2021, 60, 53–65.(d)Holtrop F; Jupp A; Slootweg JC Radicals in frustrated Lewis pair chemistry. *Springer, Cham*, 2021. pp. 361–385.
- (13). (a)Charles III RM; Brewster TP H₂ and carbon-heteroatom bond activation mediated by polarized heterobimetallic complexes. *Coord. Chem. Rev.* 2021, 433, 213765. [PubMed: 35418712] (b)Hicken A; White AJP; Crimmin MR Selective Reduction of CO₂ to a Formate Equivalent with Heterobimetallic Gold-Copper Hydride Complexes. *Angew. Chem., Int. Ed.* 2017, 56, 15127–15130.(c)Mankad NP Selectivity Effects in Bimetallic Catalysis. *Chem. - Eur. J.* 2016, 22, 5822–5829. [PubMed: 26879884] (d)Bagherzadeh S; Mankad NP Catalyst Control of Selectivity in CO₂ Reduction Using a Tunable Heterobimetallic Effect. *J. Am. Chem. Soc.* 2015, 137, 10898–10901. [PubMed: 26293355] (e)Chipman JA; Berry JF Paramagnetic Metal-Metal Bonded Heterobimetallic Complexes. *Chem. Rev.* 2020, 120, 2409–2447. [PubMed: 32045223] (f)Power PP Main-group elements as transition metals. *Nature* 2010, 463, 171–177. [PubMed: 20075912]
- (14). (a)Lai Q; Bhuvanesh N; Ozerov OV Unexpected B/Al Transelementation within a Rh Pincer Complex. *J. Am. Chem. Soc.* 2020, 142, 20920–20923. [PubMed: 33263407] (b)Hara N; Saito T; Semba K; Kuriakose N; Zheng H; Sakaki S; Nakao Y Rhodium Complexes Bearing PAIP Pincer Ligands. *J. Am. Chem. Soc.* 2018, 140, 7070–7073. [PubMed: 29792688] (c)Ekkert O; White AJP; Toms H; Crimmin MR Addition of Aluminium, Zinc and Magnesium Hydrides to Rhodium(III). *Chem. Sci.* 2015, 6, 5617–5622. [PubMed: 28757949] (d)Lai Q; Cosio MN; Ozerov OV Ni Complexes of an Alane/Tris(phosphine) Ligand Built Around a Strongly Lewis Acidic Tris(N-pyrrolyl)aluminum. *Chem. Commun.* 2020, 56, 14845–14848.
- (15). Anand BN; Krossing I; Nöth H Synthesis and X-Ray Crystal Structure of (Tmp)₂Al-Fe(Cp)(CO)₂: An Alanyl-Containing Iron Complex with a Tricoordinated Aluminum Atom. *Inorg. Chem.* 1997, 36, 1979–1981. [PubMed: 11669807]
- (16). Braunschweig H; Müller J; Ganter B Molecular Structure of [CpFe(CO)₂]₂AlAr (Ar = 2-[(Dimethylamino)methyl]phenyl): An Alanediyl Complex with Two Fe-Al Bonds. *Inorg. Chem.* 1996, 35, 7443–7444. [PubMed: 11666941]
- (17). Mears KL; Stennett CR; Taskinen EK; Knapp CE; Carmalt CJ; Tuononen HM; Power PP Molecular Complexes Featuring Unsupported Dispersion-Enhanced Aluminum-Copper and Gallium-Copper Bonds. *J. Am. Chem. Soc.* 2020, 142, 19874–19878. [PubMed: 33170691]
- (18). Liu H-Y; Schwamm RJ; Hill MS; Mahon MF; McMullin CL; Rajabi NA Ambiphilic Al-Cu Bonding. *Angew. Chem., Int. Ed.* 2021, 60, 14390–14393.
- (19). Rudd PA; Liu S; Gagliardi L; Young VG; Lu CC Metal-Alane Adducts with Zero-Valent Nickel, Cobalt, and Iron. *J. Am. Chem. Soc.* 2011, 133, 20724–20727. [PubMed: 22122804]
- (20). Kong RY; Crimmin MR 1st row transition metal aluminylene complexes: preparation, properties and bonding analysis. *Dalton Trans.* 2021, 50, 7810–7817. [PubMed: 34002191]

- (21). Hicks J; Mansikkamäki A; Vasko P; Goicoechea JM; Aldridge S A Nucleophilic Gold Complex. *Nat. Chem.* 2019, 11, 237–241 [PubMed: 30664716]
- (22). Sorbelli D; Belpassi L; Belanzoni P Reactivity of a Gold-Alumanyl Complex with Carbon Dioxide: A Nucleophilic Gold? *J. Am. Chem. Soc.* 2021, 143, 14433–14437. [PubMed: 34472349]
- (23). McManus C; Hicks J; Cui X; Zhao L; Frenking G; Goicoechea JM; Aldridge S Coinage metal alumanyl complexes: probing regiochemistry and mechanism in the insertion and reduction of carbon dioxide. *Chem. Sci.* 2021, 12, 13458–13468. [PubMed: 3477765]
- (24). Roy MMD; Hicks J; Vasko P; Helimann A; Baston A-M; Goicoechea JM; Aldridge S Probing the Extremes of Covalency in M–Al bonds: Lithium and Zinc Alumanyl Compounds. *Angew. Chem., Int. Ed.* 2021, 60, 22301–22306.
- (25). (a)Fischer RA; Priermeier T Transition-Metal-Substituted Alanes: Synthesis and Spectroscopic Studies and the Structure of $(\eta^5\text{-C}_5\text{H}_5)(\text{CO})_2\text{Fe-Al}[(\text{CH}_2)_3\text{NMe}_2](\text{iBu})$. *Organometallics* 1994, 13, 4306–4314.(b)Jones C; Aldridge S; Gans-Eichler T; Stasch A Synthesis and characterisation of complexes of Group 13 metal amidinate heterocycles with the $\text{CpFe}(\text{CO})_2$ fragment. *Dalton Trans.* 2006, 5357–5361. [PubMed: 17102861] (c)Riddlestone IM; Urbano J; Phillips N; Kelly MJ; Vidovic D; Bates JI; Taylor R; Aldridge S Salt Metathesis for the Synthesis of M-Al and M-H-Al Bonds. *Dalton Trans.* 2013, 42, 249–258. [PubMed: 23069776] (d)Yanagisawa T; Mizuhata Y; Tokitoh N Dibromometallyl-iron complexes generated by the recombination of an alumanyl-iron complex with EBr_3 (E = Al, Ga). *Heteroat. Chem.* 2018, 29, e21465.(e)Agou T; Yanagisawa T; Sasamori T; Tokitoh N Synthesis and Structure of an Iron-Bromoalumanyl Complex with a Tri- Coordinated Aluminum Center. *Bull. Chem. Soc. Jpn.* 2016, 89, 1184–1186.(f)Weiss J; Stetzkamp D; Nuber B; Fischer RA; Boehme C; Frenking G [$(\eta^5\text{-C}_5\text{Me}_5)\text{Al-Fe}(\text{CO})_4$]-Synthesis, Structure, and Bonding. *Angew. Chem., Int. Ed. Engl.* 1997, 36, 70–72.
- (26). Whiteoak CJ; Kielland N; Laserna V; Escudero-Adán EC; Martin E; Kleij AW A Powerful Aluminum Catalyst for the Synthesis of Highly Functional Organic Carbonates. *J. Am. Chem. Soc.* 2013, 135, 1228–1231. [PubMed: 23302007]
- (27). Pinkes JR; Steffey BD; Vites JC; Cutler AR Carbon Dioxide Insertion into the Fe-Zr and Ru-Zr Bonds of the Heterobimetallic Complexes $\text{Cp}(\text{CO})_2\text{M-Zr}(\text{Cl})\text{Cp}_2$: Direct Production of the $\mu\text{-}\eta^1(\text{C}): \eta^2(\text{O}, \text{O}')\text{-CO}_2$ Compounds $\text{Cp}(\text{CO})_2\text{M-CO}_2\text{-Zr}(\text{Cl})\text{Cp}_2$. *Organometallics* 1994, 13, 21–23.
- (28). Lamb JR; Hubbell AK; MacMillan SN; Coates GW Carbonylative, Catalytic Deoxygenation of 2,3-Disubstituted Epoxides with Inversion of Stereochemistry: An Alternative Alkene Isomerization Method. *J. Am. Chem. Soc.* 2020, 142, 8029–8035. [PubMed: 32309937]
- (29). Memmler H; Kauper U; Gade LH; Scowen IJ; McPartlin M Insertion of $\text{X} = \text{C}=\text{Y}$ Heteroallenes into Unsupported Zr-M Bonds (M = Fe, Ru). *Chem. Commun.* 1996, 15, 1751–1752.
- (30). Friedrich HB; Onani MO; Rademeyer M Bromopropylidicarbonyl(η^5 -pentamethylcyclopentadienyl)iron(II). *Acta Cryst. E* 2004, 60, m551–m553.
- (31). Giannini L; Solari E; Angelis SD; Ward TR; Floriani C; Chiesi-Villa A; Rizzoli C Migratory Aptitude of the Zr-C Functionalities Bonded to a Macrocyclic Structure: Thermally- and Solvent-assisted Intra- and Intermolecular Migrations in Dialkyl(dibenzotetramethyltetraazaannulene)zirconium(IV). *J. Am. Chem. Soc.* 1995, 117, 5801–5811.
- (32). Camp C; Arnold J On the non-innocence of "Nacnacs": ligand-based reactivity in β -diketiminato supported coordination compounds. *Dalton Trans.* 2016, 45, 14462–14498. [PubMed: 27353604]
- (33). (a)Foster JP; Weinhold F Natural hybrid orbitals. *J. Am. Chem. Soc.* 1980, 102, 7211–7218. (b)Reed AE; Weinhold F Natural bond orbital analysis of near-Hartree-Fock water dimer. *J. Chem. Phys.* 1983, 78, 4066–4073.
- (34). (a)Bader RFW A quantum theory of molecular structure and its applications. *Chem. Rev.* 1991, 91, 893–928.(b)Bader RFW Atoms in Molecules. A Quantum Theory (Oxford Univ. Press, Oxford, 1994), pp. 1–458.
- (35). Laidig KE; Bader RFW Properties of Atoms in Molecules: Atomic Polarizabilities. *J. Chem. Phys.* 1990, 93, 7213–7224.

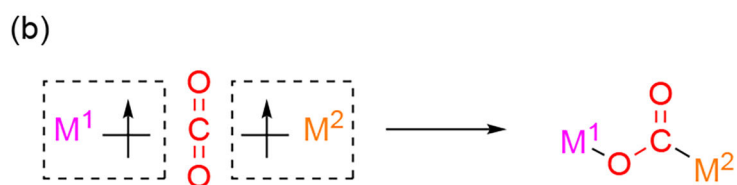
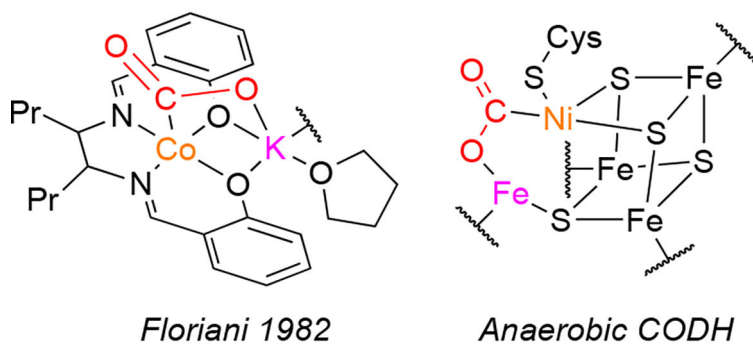
- (36). Jayarathne U; Mazzacano TJ; Bagherzadeh S; Mankad NP Heterobimetallic Complexes with Polar, Unsupported Cu-Fe and Zn-Fe Bonds Stabilized by N-Heterocyclic Carbenes. *Organometallics* 2013, 32, 3986–3992.
- (37). (a) Wiberg KB Application of the pople-santry-segal CNDO method to the cyclopropylcarbinyl and cyclobutyl cation and to bicyclobutane. *Tetrahedron* 1968, 24, 1083–1096. (b) Sizova OV; Skripnikov LV; Sokolov AY Symmetry decomposition of quantum chemical bond orders, *J. Mol. Struct. (Theochem)* 2008, 870, 1–3, 1–9.
- (38). Pinkes John R.; Masi Christopher J.; Chiulli Robert; Steffey Bryan D.; Cutler AR Carbon Dioxide Complexation: Infrared Spectroscopy of Iron and Ruthenium η^5 -Cyclopentadienyl Carbonyl Metallo-carboxylates. *Inorg. Chem.* 1997, 36, 70–79.
- (39). Castro-Rodriguez I; Nakai H; Zakharov LN; Rheingold AL; Meyer K A linear, O-Coordinated η^1 -CO₂ Bound to Uranium. *Science* 2004, 305, 1757–1759. [PubMed: 15375263]
- (40). Saouma CT; Lu CC; Day MW; Peters JC CO₂ reduction by Fe(I): solvent control of C–O cleavage *versus* C–C coupling *Chem. Sci.* 2013, 4, 4042–4051.
- (41). Falconer RL; Nichol GS; Smolyar IV; Cockroft SL; Cowley MJ. Reversible Reductive Elimination in Aluminum(II) Dihydrides. *Angew. Chem. Int. Ed.* 2021, 60, 2047–2052.
- (42). Marquard SL; Bezpalko MW; Foxman BM; Thomas CM Stoichiometric C=O Bond Oxidative Addition of Benzophenone by a Discrete Radical Intermediate To Form a Cobalt(I) Carbene. *J. Am. Chem. Soc.* 2013, 135, 6018–6021. [PubMed: 23574005]
- (43). Murphy DM; McDyre LE; Carter E; Stasch A; Jones C A CW-EPR, ENDOR and special TRIPLE resonance study of a novel magnesium ketyl radical. *Magn. Reson. Chem.* 2011, 49, 159–163. [PubMed: 21243724]
- (44). (a) Mailer C; Hoffman BM Tumbling of an adsorbed nitroxide using rapid adiabatic passage. *J. Phys. Chem.* 1976, 80, 842–846. (b) Mailer C; Taylor CPS Rapid Adiabatic Passage EPR of Ferricytochrome c: Signal Enhancement and Determination of Spin-Lattice Relaxation Time. *Biochim. Biophys. Acta, Protein Struct.* 1973, 322, 195–203.
- (45). Hyde JS; Froncisz W The Role of Microwave Frequency in EPR Spectroscopy of Copper Complexes. *Ann. Rev. of Biophys. and Bioeng.* 1982 11:1, 391–417. [PubMed: 6285804]
- (46). (a) Kundu S; Sinhababu S; Dutta S; Mondal T; Koley D; Dittrich B; Schwederski B; Kaim W; Stuckl AC; Roesky HW Synthesis and characterization of Lewis base stabilized mono- and di-organo aluminum radicals. *Chem. Commun.* 2017, 53, 10516–10519. (b) Li B; Kundu S; Stuckl AC; Zhu H; Keil H; Herbst-Irmer R; Stalke D; Schwederski B; Kaim W; Andrada DM; Frenking G; Roesky HW A stable neutral radical in the coordination sphere of aluminum. *Angew. Chem., Int. Ed.* 2017, 56, 397–400. (c) Siddiqui MM; Banerjee S; Bose S; Sarkar SK; Gupta SK; Kretsch J; Graw N; Herbst-Irmer R; Stalke D; Dutta S; Koley D; Roesky HW Cyclic (Alkyl)(Amino)Carbene-Stabilized Aluminum and Gallium Radicals Based on Amidinate Scaffolds. *Inorg. Chem.* 2020, 59, 11253–11258. [PubMed: 32799492]
- (47). Rao G; Altman AB; Brown AC; Tao L; Stich TA; Arnold J; Britt RD Metal Bonding with 3d and 6d Orbitals: An EPR and ENDOR Spectroscopic Investigation of Ti³⁺⁺-Al and Th³⁺⁺-Al Heterobimetallic Complexes. *Inorg. Chem.* 2019, 58, 7978–7988. [PubMed: 31185562]
- (48). Morton JR; Preston KF Atomic parameters for paramagnetic resonance data. *J. Magn. Reson.* 1978, 30, 577–582.
- (49). (a) Adamo C; Barone V Toward reliable density functional methods without adjustable parameters: The PBE0 model. *J. Chem. Phys.* 1999, 110, 6158–6169. (b) Grimme S; Ehrlich S; Goerigk L Effect of the damping function in dispersion corrected density functional theory. *J. Comp. Chem.* 2011, 32, 1456–1465. [PubMed: 21370243] (c) Weigend F; Ahlrichs R Balanced basis sets of split valence, triple zeta valence and quadruple zeta valence quality for H to Rn: Design and assessment of accuracy. *Phys. Chem. Phys.* 2005, 7, 3297–3305. [PubMed: 16240044] (d) Marenich AV; Cramer CJ; Truhlar DG; Universal solvation model based on solute electron density and a continuum model of the solvent defined by the bulk dielectric constant and atomic surface tensions. *J. Phys. Chem. B* 2009, 113, 6378–6396. [PubMed: 19366259]
- (50). Gaussian 16, Revision B.01, Frisch MJ; Trucks GW; Schlegel HB; Scuseria GE; Robb MA; Cheeseman JR; Scalmani G; Barone V; Petersson GA; Nakatsuji H; Li X; Caricato M; Marenich AV; Bloino J; Janesko BG; Gomperts R; Mennucci B; Hratchian HP; Ortiz JV; Izmaylov AF; Sonnenberg JL; Williams-Young D; Ding F; Lipparini F; Egidi F; Goings J; Peng B; Petrone

A; Henderson T; Ranasinghe D; Zakrzewski VG; Gao J; Rega N; Zheng G; Liang W; Hada M; Ehara M; Toyota K; Fukuda R; Hasegawa J; Ishida M; Nakajima T; Honda Y; Kitao O; Nakai H; Vreven T; Throssell K; Montgomery JA Jr.; Peralta JE; Ogliaro F; Bearpark MJ; Heyd JJ; Brothers EN; Kudin KN; Staroverov VN; Keith TA; Kobayashi R; Normand J; Raghavachari K; Rendell AP; Burant JC; Iyengar SS; Tomasi J; Cossi M; Millam JM; Klene M; Adamo C; Cammi R; Ochterski JW; Martin RL; Morokuma K; Farkas O; Foresman JB; Fox DJ Gaussian, Inc., Wallingford CT, 2016.

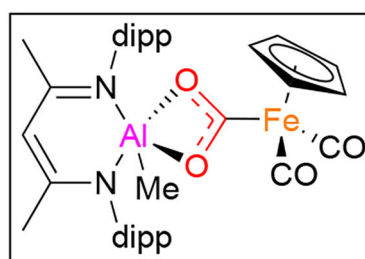
- (51). NBO Version 3.1, Glendening ED; Reed AE; Carpenter JE; Weinhold F Theoretical Chemistry Institute, University of Wisconsin, Madison, 2003.
- (52). Lu T; Chen F Multiwfn: A Multifunctional Wavefunction Analyzer. *J. Comput. Chem.* 2012, 33, 580–592. [PubMed: 22162017]



Cooperative CO₂ reduction: 2e⁻ from Lewis base, anion stabilization by Lewis acid



Radical pair pathway: 1e⁻ each from two metalloradicals



This work

Figure 1. Cooperative CO₂ activation pathways and representative examples: (a) Lewis acid/base bifunctionality, (b) radical pair chemistry (this work).

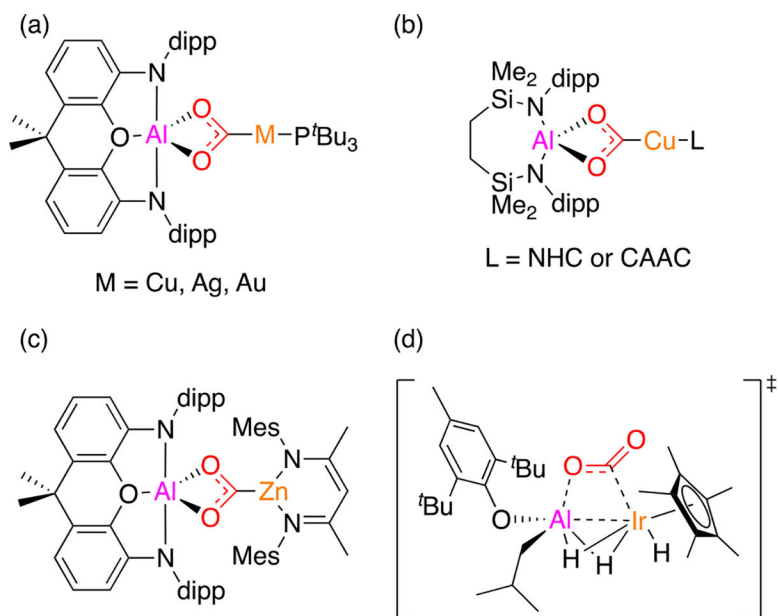


Figure 2. Previously reported examples of complexes derived from CO_2 insertion into Al-M bonds.

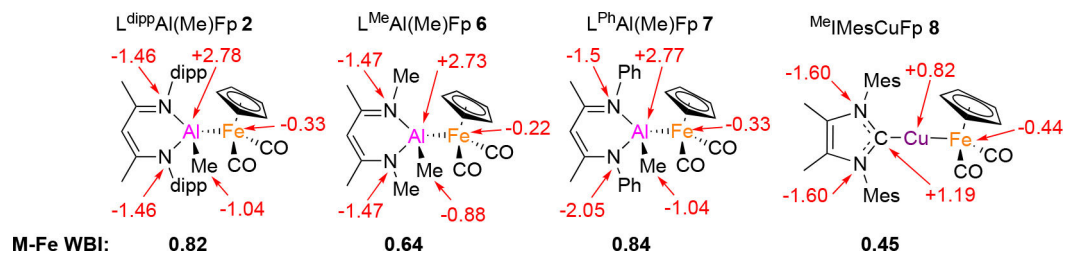


Figure 3. Calculated QTAIM charges (red) for selected atoms in **2** and **6-8**, with M-Fe Wiberg bond indices (black) indicated below the structures.

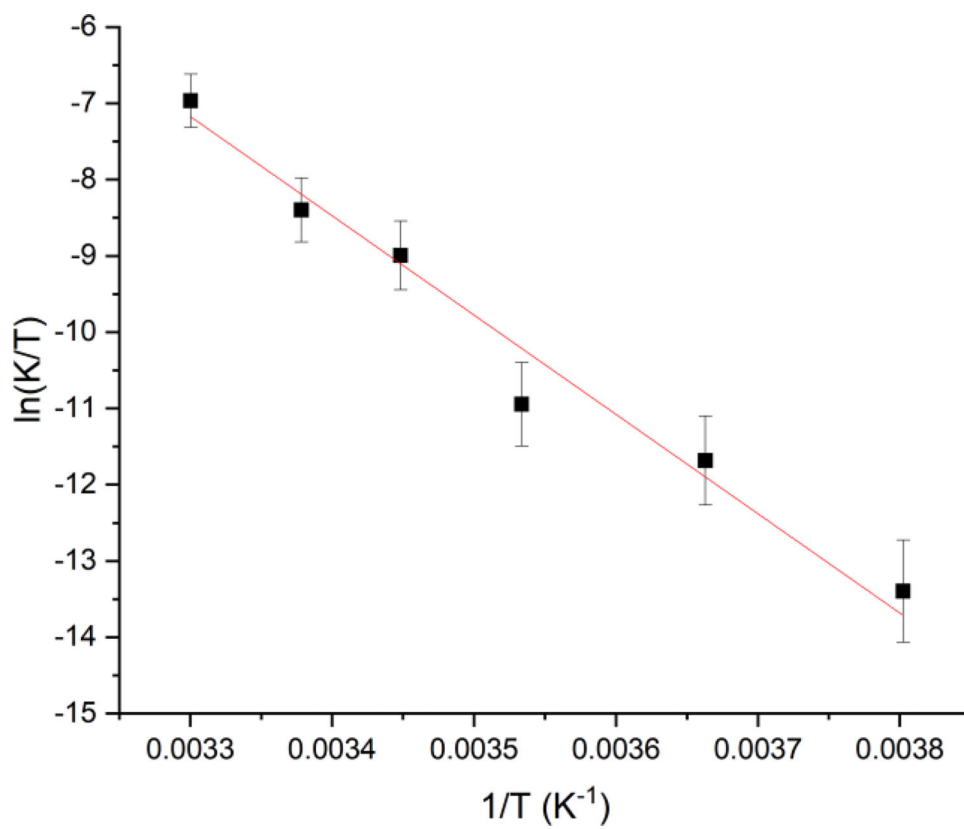
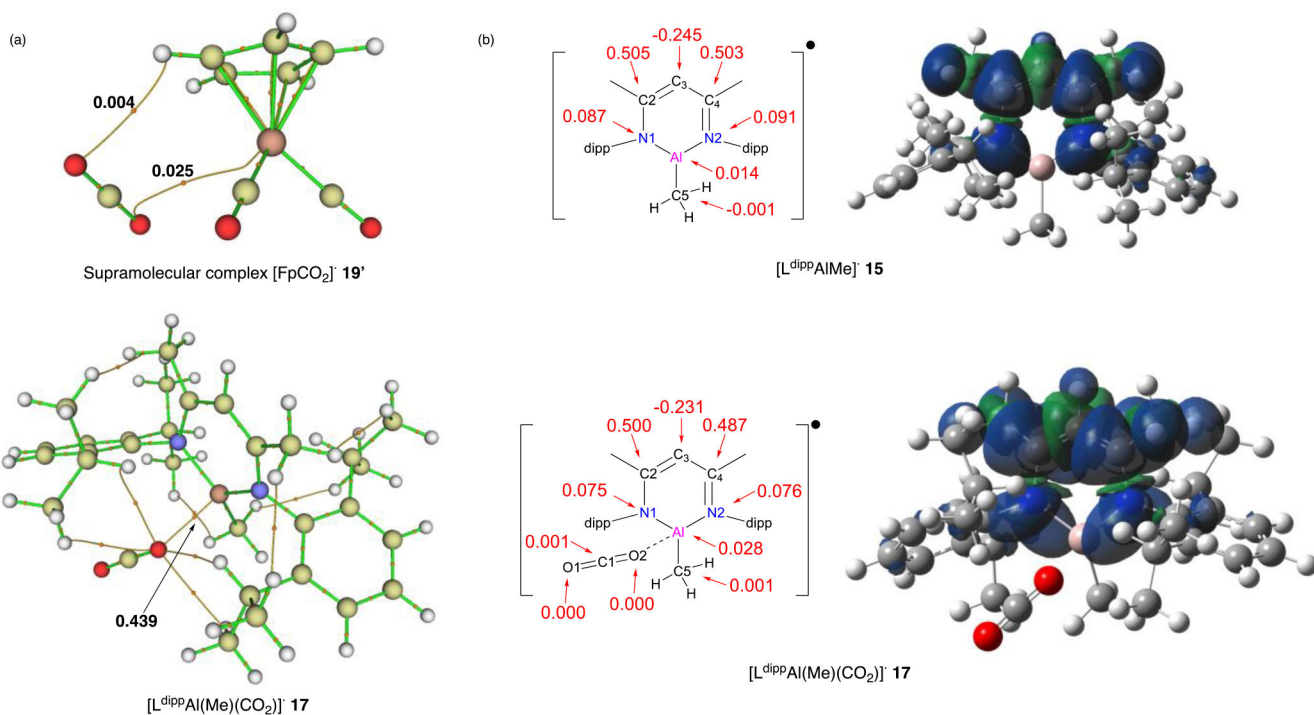
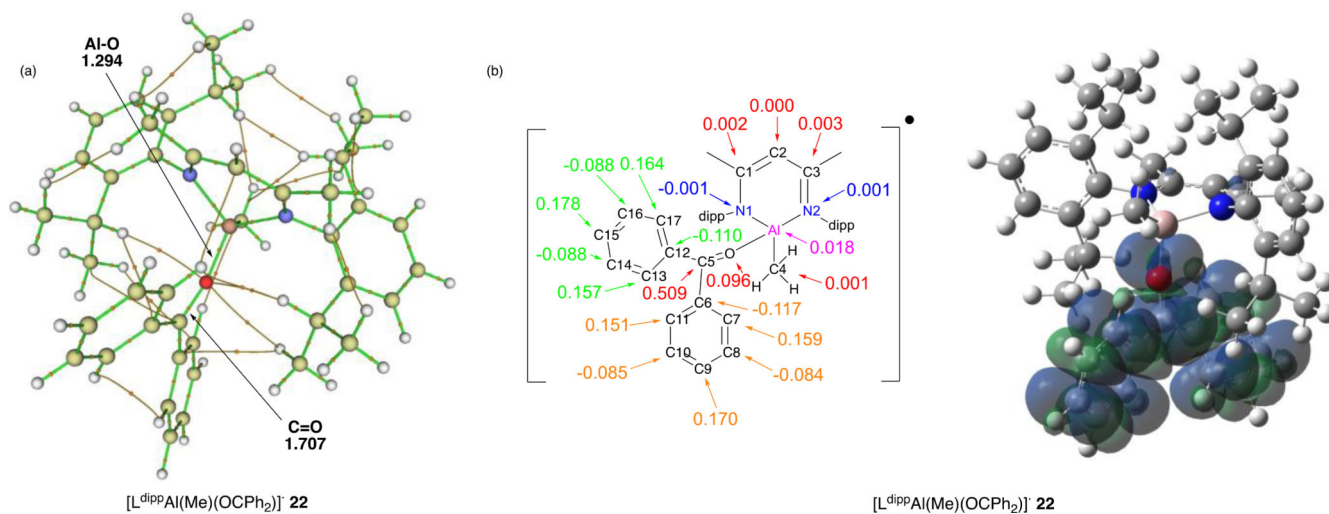


Figure 4. Eyring analysis to extract activation parameters for the CO₂ activation reaction by **2**.

**Figure 5.**

(a) Selected QTAIM paths connecting (3,-3) and (3,-1) critical points for $\mathbf{19}'$ and $\mathbf{17}$ with key all-electron Wiberg bond indices shown; (b) calculated Mulliken spin densities for selected atoms and corresponding spin density plots (isosurface value = 0.0004) for $\mathbf{15}$ and $\mathbf{17}$.

**Figure 6.**

(a) Selected QTAIM paths connecting (3,-3) and (3,-1) critical points for **22** with key all-electron Wiberg bond indices shown; (b) calculated Mulliken spin densities for selected atoms and corresponding spin density plot (isosurface value = 0.0004) for **22**.

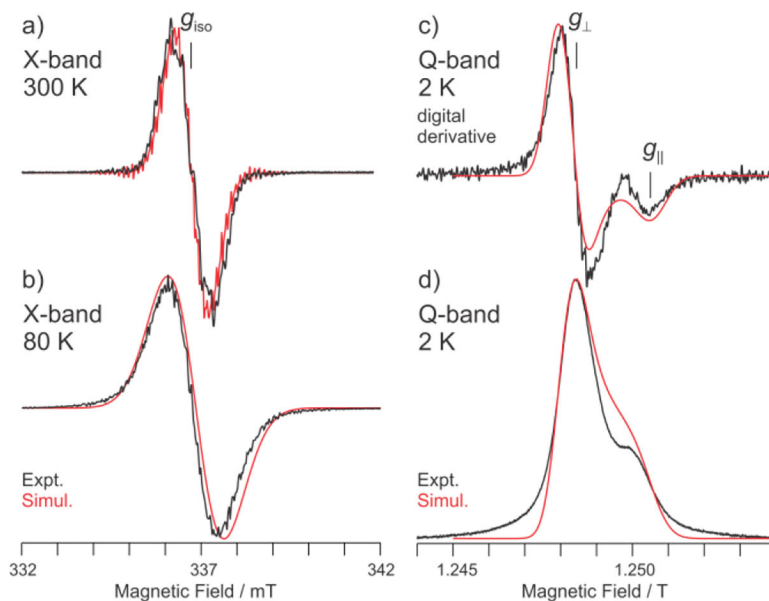


Figure 7.

EPR spectra (black traces) of **22** in toluene solution with simulations (red traces): a) X-band spectrum recorded at ambient temperature; microwave frequency, 9.45999 GHz; field modulation amplitude, 0.1 mT; time constant, 20 ms; b) X-band spectrum recorded at 80 K, conditions as in (a) except microwave frequency, 9.456414 GHz; c) digital derivative of Q-band spectrum; d) (passage conditions) Q-band spectrum recorded at 2 K; microwave frequency, 35.0530 GHz; microwave power, 2 μ W; field modulation amplitude, 0.2 mT; time constant, 32 ms; scan time, 120 s. Simulation parameters: a) $g = 2.006$, sum of $W = 16$ MHz (Gaussian hwhm) no hfc and $W = 0.5$ MHz with $a_{\text{iso}}(^{27}\text{Al}) = 4$ MHz; $a_{\text{iso}}(\text{o-}^1\text{H}) \times 4 = 22$ MHz; $a_{\text{iso}}(\text{m-}^1\text{H}) \times 4 = 7.5$ MHz; $a_{\text{iso}}(\text{p-}^1\text{H}) \times 2 = 26$ MHz; The contribution of the simulation with hfc to that without was visually scaled to match experiment and has no quantitative relevance; b) $g = [2.0075, 2.0066, 2.0032]$, $W = 25$ MHz; c) and d) $g = [2.0070, 2.0061, 2.0027]$, $W = 14, 10, 10$ MHz. This g tensor reflects actual g anisotropy resolved in the rigid matrix and was used in (b), with a slight shift in g values to account for magnetic field imprecision (< 0.1 mT). The features corresponding to $g_{\parallel} = 2.0027$ and $g_{\perp} \approx 2.0065$ are indicated.

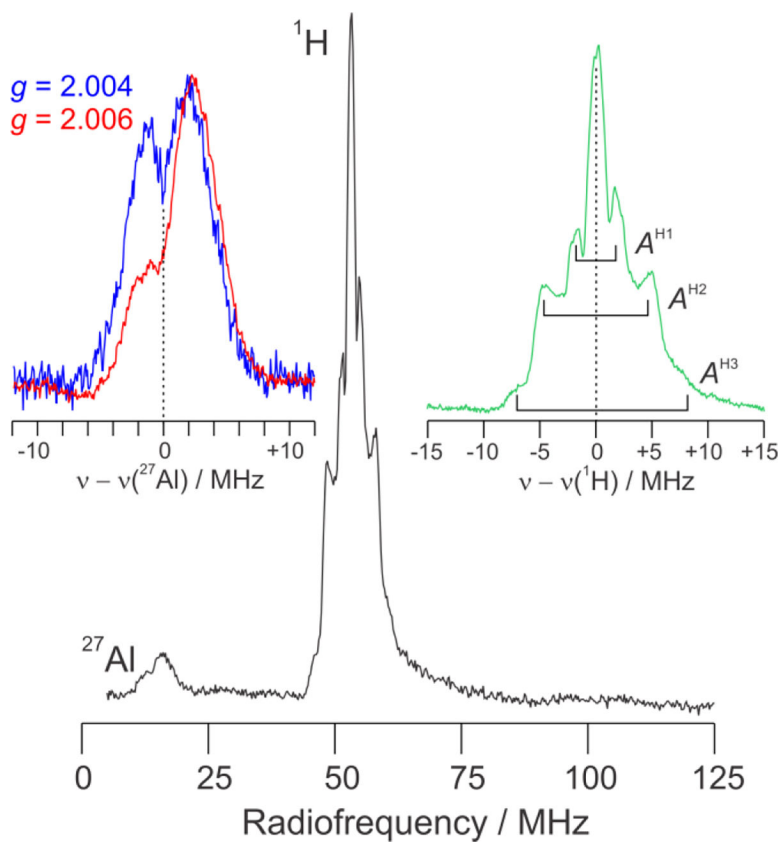
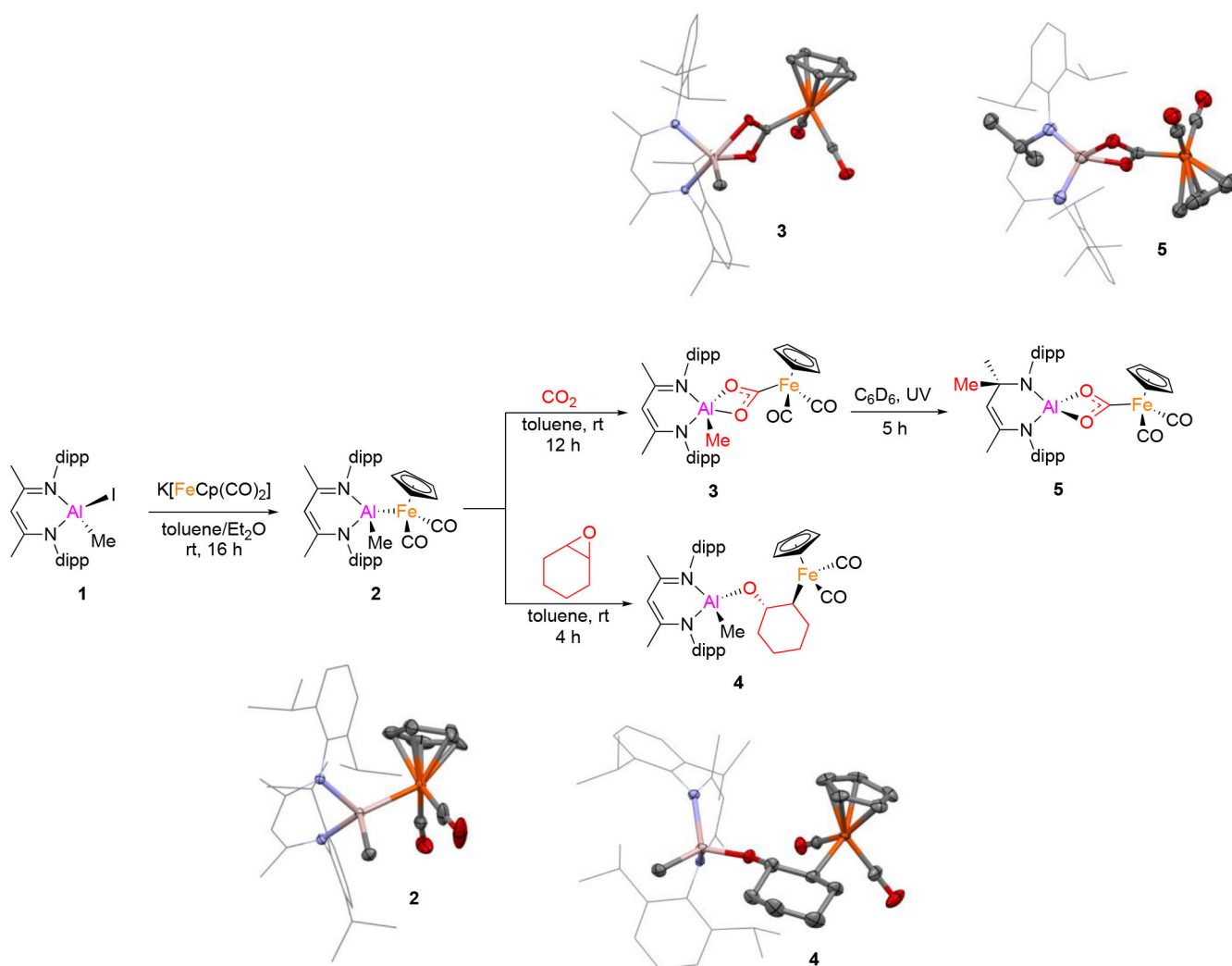
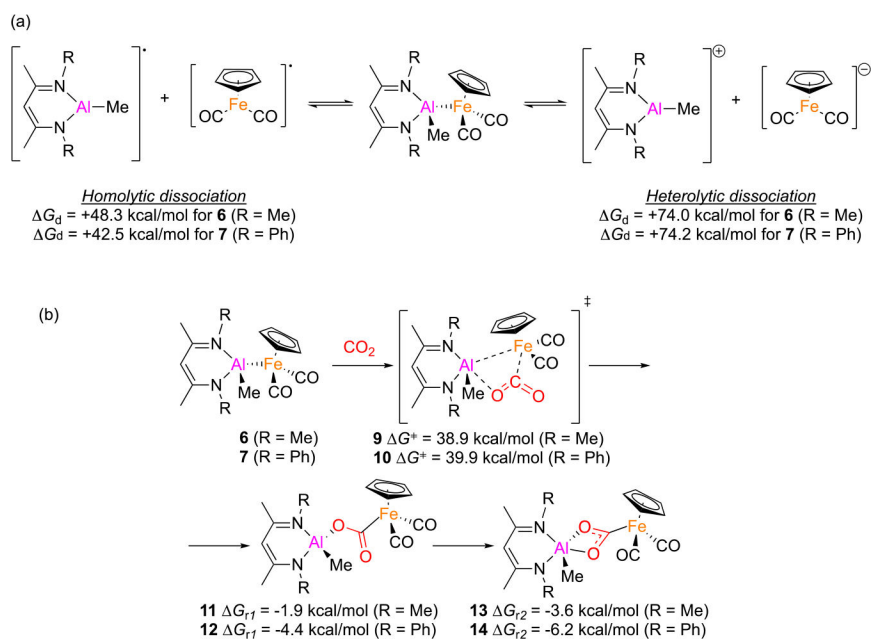


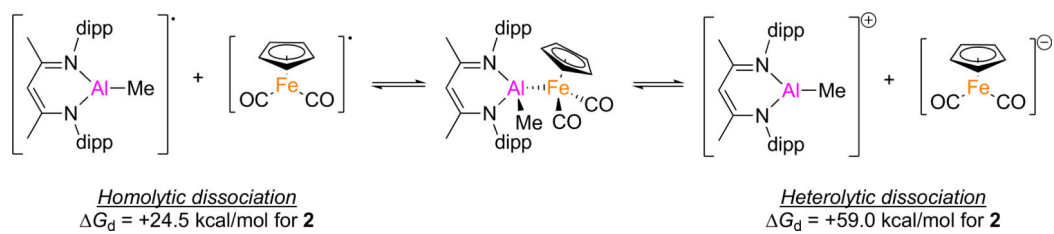
Figure 8. CW 35 GHz ENDOR spectra of **22** in toluene solution. Experimental conditions: 35.0530 GHz; microwave power, 2 μ W; field modulation amplitude, 0.1 mT; time constant, 32 ms; magnetic field, 1.2484 T ($g = 2.0061$); radiofrequency(rf) scan rate, 1 MHz/s; 3 scans, The spectra shown in the insets used the same conditions except in the ^{27}Al spectra: field modulation, 0.2 mT; 20 scans; and the spectrum shown in blue had magnetic field, 1.2497 T ($g = 2.0040$).

**Scheme 1.**

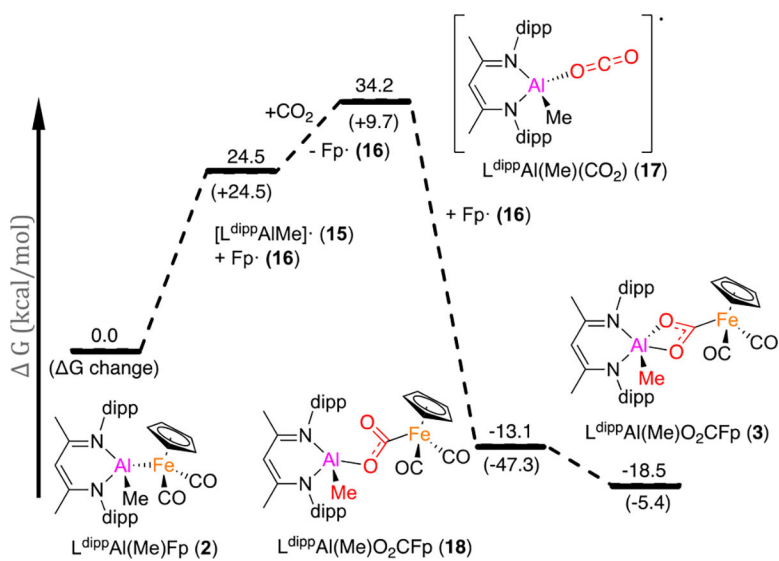
Thermal and photochemical reactivity studies of an Al-Fe heterobinuclear system, including solid-state structures of complexes **2-5** determined by X-ray crystallography. For clarity, hydrogen atoms and co-crystallized solvent molecules are omitted from the crystal structures; ligand backbones (except nitrogen) are shown as wireframes, and all other atoms are shown as 50% probability ellipsoids.

**Scheme 2.**

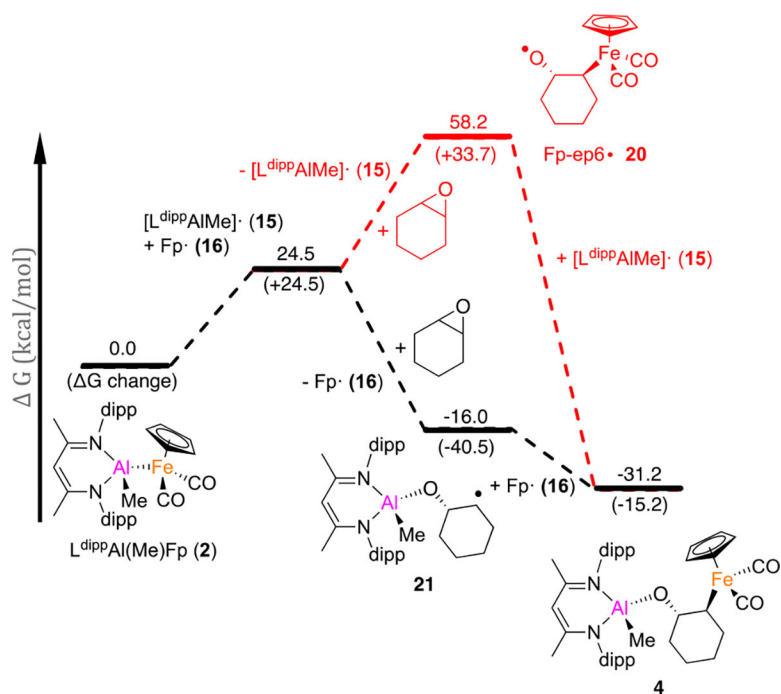
Unscaled Gibbs free energies (PBE1PBE) for (a) Al-Fe bond dissociation and (b) concerted CO₂ insertion pathways.

**Scheme 3.**

Gibbs free energies (PBE1PBE) for Al-Fe bond dissociation of **2**.

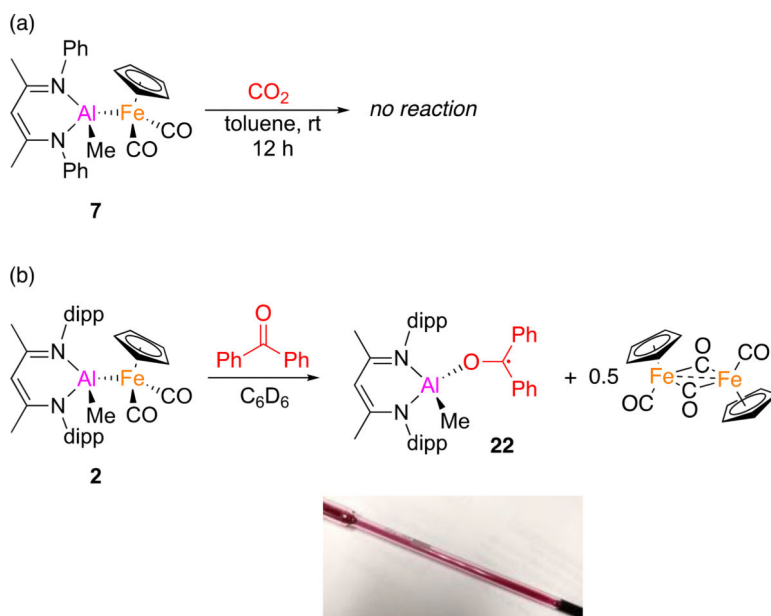
**Scheme 4.**

Gibbs free energy diagram for calculated pathways of CO_2 activation mediated by **2**.



Scheme 5.

Gibbs free energy diagrams for calculated pathways of cyclohexene oxide ring opening mediated by **2**.

**Scheme 6.**

(a) Experimental validation of a computational prediction, and (b) direct observation of the purple Al-containing radical, $L^{\text{dipp}}\text{Al}(\text{Me})(\text{OCPh}_2)$, **22**.